FULL PAPER

PbS/CdS/ZnS Quantum Dots: A Multifunctional Platform for In Vivo Near-Infrared Low-Dose Fluorescence Imaging

Antonio Benayas, Fuqiang Ren, Elisa Carrasco, Vicente Marzal, Blanca del Rosal, Belete A. Gonfa, Ángeles Juarranz, Francisco Sanz-Rodríguez, Daniel Jaque, José García-Solé, Dongling Ma,* and Fiorenzo Vetrone**

Over the past decade, near-infrared (NIR)-emitting nanoparticles have increasingly been investigated in biomedical research for use as fluorescent imaging probes. Here, high-quality water-dispersible core/shell/shell PbS/CdS/ZnS quantum dots (hereafter QDs) as NIR imaging probes fabricated through a rapid, cost-effective microwave-assisted cation exchange procedure are reported. These QDs have proven to be water dispersible, stable, and are expected to be nontoxic, resulting from the growth of an outer ZnS shell and the simultaneous surface functionalization with mercaptopropionic acid ligands. Care is taken to design the emission wavelength of the QDs probe lying within the second biological window (1000–1350 nm), which leads to higher penetration depths because of the low extinction coefficient of biological tissues in this spectral range. Furthermore, their intense fluorescence emission enables to follow the real-time evolution of QD biodistribution among different organs of living mice, after low-dose intravenous administration. In this paper, QD platform has proven to be capable (ex vivo and in vitro) of high-resolution thermal sensing in the physiological temperature range. The investigation, together with the lack of noticeable toxicity from these PbS/CdS/ZnS QDs after preliminary studies, paves the way for their use as outstanding multifunctional probes both for in vitro and in vivo applications in biomedicine.

1. Introduction

The relevance and need for extending the range of in vivo optical imaging in biomedicine, both for disease screening and image-guided surgical interventions, require robust and intense, nanoscale emitters. Of particular importance, their emitted optical signal must be capable of passing through living tissues, allowing for the acquisition of images deep within the tissue, using portable, cost effective, and real-time sensing systems.[1] Clearly, selection of the emission wavelength is a critical parameter, and designing and implementing a nanoprobe that offers multifunctionality could revolutionize modern medicine, as it would minimize the diversity of detection/therapeutic agents to be used.[2] A subset of optical nanoprobes is capable of providing multiparameter local information in a living biological environment. Among the diverse information modes reported by these multifunctional optical nanoprobes,

Dr. A. Benayas, F. Ren, B. A. Gonfa, Prof. D. Ma, Prof. F. Vetrone
Institut National de la Recherche Scientifique–Énergie Matériaux et Télécommunications
Université du Québec
1650 Boul. Lionel-Boulet, Varennes, QC J3X 1S2, Canada
E-mail: ma@emt.inrs.ca; vetrone@emt.inrs.ca
Dr. E. Carrasco, Prof. Á. Juarranz
Instituto de Investigaciones Biomédicas "Alberto Sols"
CSIC-UAM
Madrid 28029, Spain
Dr. E. Carrasco, Prof. Á. Juarranz, Prof. F. Sanz-Rodríguez
Departamento de Biología
Facultad de Ciencias
Universidad Autónoma de Madrid
Campus de Cantoblanco
Madrid 28049, Spain
Dr. E. Carrasco, Prof. Á. Juarranz, Prof. D. Jaque
Instituto Ramón y Cajal de Investigación Sanitaria
Hospital Universitario Ramón y Cajal
Madrid 28034, Spain
E-mail: daniel.jaque@uam.es
V. Marzal, B. del Rosal, Prof. D. Jaque, Prof. J. García-Solé
Fluorescence Imaging Group
Departamento de Física de Materiales
Facultad de Ciencias
Universidad Autónoma de Madrid
Campus de Cantoblanco
Madrid 28049, Spain
B. del Rosal, Prof. D. Jaque, Prof. J. García-Solé
Instituto Nicolás Cabrera
Facultad de Ciencias
Universidad Autónoma de Madrid
Campus de Cantoblanco, Madrid 28049, Spain
Prof. F. Vetrone
Centre for Self-Assembled Chemical Structures
McGill University
Montreal, QC H3A 2K6, Canada

DOI: 10.1002/adfm.201502632

temperature is one of the most significant.[3] The great majority of diseases, both at the cellular and the tissue level, have an immediate thermal related effect. So, to accurately ascertain the location of thermal abnormalities is an invaluable tool for early detection of medical problems as well as for real-time monitoring of ongoing medical therapies and interventions. If a multifunctional fluorescence nanoprobe is to be used for in vivo thermometry, it has, first, to be capable of deep tissue imaging and, simultaneously, it must show fluorescence that is strongly dependent on temperature. These two conditions are, typically, hard to find in a single nanostructure.

Presently, among the fluorescent nanoplatforms studied for biomedical applications, there has been a great deal of interest in semiconductor quantum dots (QDs), due to their interesting optical properties, such as high emission intensity and size-based tunability.[4] To render them even more versatile for widespread adoption in biomedicine, a large body of research is now focused on developing QDs emitting in the near-infrared (NIR) region. A wave of recently published work suggests that the NIR spectral windows (700–950 and 1000–1350 nm) can improve the sensitivity of in vivo imaging.[5–9] This is based on the fact that working in these spectral windows ensures the optimization of the intrabody light penetration depth.[10,11] This is caused by the lower optical interaction (extinction) between the NIR photons and the biological tissues. In the "first biological window" (700–950 nm), the light is minimally absorbed by tissue components as compared to visible light, resulting in greater penetration and thus deeper imaging.[12] At even longer wavelengths, a greater reduction in the scattering cross section leads to a further improvement in the detection depth and resolution.[6,13,14] This region, between 1000 and 1350 nm, is subsequently defined as the "second biological window."[10,14] The interest in imaging in this second biological window, which is hard to achieve using traditional biomarkers (such as dye molecules and fluorescent proteins), has shifted research efforts from the widely used Cd^{2+}-based QDs to Pb^{2+}-based chalcogenides. Specifically, PbS, PbSe, and PbTe QDs have attracted a great deal of attention owing to their unique features, such as narrower band gaps resulting in emission in both biological windows, and larger Bohr radii with respect to other QDs.[15] The combination of the small bulk band gap and large Bohr radius yields a wide tunability of the electronic states.[16–18] These QDs emit brightly, making them a very attractive option among NIR fluorescence probes.[19,20]

Nevertheless, the issue of toxicity remains a strong concern when utilizing lead/cadmium-based QDs for biological applications. Any nanostructured material that is projected for use inside living specimens should mandatorily address a number of questions regarding its potential to disrupt the normal development of biological processes. Moreover, care must be taken to ascertain if any accumulation of toxic residues exists in the body and its possible long-term consequences. These issues become especially relevant if the substances used are heavy metals, as they are known to cause adverse health effects if accumulated inside of a living organism.[21] However, despite concerns regarding their toxicity, reports have recently emerged that are changing the initial perception of these materials. For instance, the work by Ye et al. focused on testing QDs in non-human primates[22] and showed that after 90 days the acute toxicity of Cd-based QDs was minimal (although the clearance of QDs from live organisms is an essential question to be addressed in future long-term studies). Such results obtained over the last few years have helped to increase the interest and focus of the research community on Cd- and Pb-based QDs as high-brightness imaging nanoprobes.[16]

In this work, we present a platform for in vivo imaging applications based on the outstanding properties of PbS/CdS/ZnS QDs. Their intense and easily detectable emission is based on the synergistic action of the PbS emitting core, the large reduction of trap states resulting from the presence of a thin, epitaxial CdS shell, and the complete isolation from the outside environment provided mainly by the robust biocompatible outer shell of ZnS. Aside from a remarkable emission intensity, the PbS/CdS/ZnS QDs can also be tuned to possess NIR emission lying within the second biological window. This allows for high penetration depths in biological tissues and was thoroughly demonstrated in our in vivo imaging experiments, which allowed us to perform real-time tracking of their biodistribution inside a living organism. Finally, our platform has demonstrated a very promising multifunctional character not only as a deep tissue imaging probe but also as a nanothermometer, capable of high-resolution fluorescence thermometry in both ex vivo and in vitro applications. These NIR fluorescent nanothermometers can be a platform for high penetration depth thermal sensing, synergistically benefiting from both high thermal sensitivity and a high penetration depth (wavelength emission perfectly matching the spectral range within the second biological window).

2. Results and Discussion

2.1. Synthesis and Surface Engineering of Biocompatible PbS/CdS/ZnS Quantum Dots

Our PbS/CdS/ZnS QDs were synthesized following two slightly different protocols, dependent upon the initial size of the starting PbS core, which is paramount in determining the spectral range of the overall core/shell/shell QD fluorescence (see Experimental Section, and Supporting Information for further details). The smallest PbS QDs, emitting within the first biological window, were synthesized using a slightly modified procedure with respect to the work of Hines et al. and Zhang et al.[18,23] In our synthesis, $Pb(OAc)_2 \cdot 3H_2O$ was used with bis(trimethylsilyl) sulfide ($(TMS)_2S$) injected at 130 °C. The largest PbS QDs were synthesized using oleylamine (OLA) as the capping ligands.[20] Both the smaller and the larger PbS cores were synthesized by the hot injection method, although the precursors, capping ligands, and injection temperature (detailed information can be found in the Supporting Information) were different. After the synthesis of the parent PbS QDs, a thin shell of CdS was grown to passivate the PbS surface using a microwave-assisted cation exchange procedure.[20] Once purified, the PbS/CdS QDs were re-dispersed in toluene followed by the rapid microwave growth of a thin ZnS outer shell where the long hydrophobic ligand (including mainly oleic acid (OA) and perhaps also a small amount of OLA) was simultaneously replaced by mercaptopropyl acid (MPA) in

order to render them dispersible in aqueous solvents. A complete description of the microwave-assisted process used to produce the MPA-capped PbS/CdS/ZnS QDs is provided in the Experimental Section (ZnS shell and MPA capping) and Supporting Information (synthesis of PbS core and PbS/CdS particles). Size analysis revealed that the average diameter of the PbS/CdS QDs was 4.6 ± 0.4 nm with an average CdS thickness of 0.35 ± 0.05 nm. Following the final growth of the outer ZnS shell, the average diameter of the 1270 nm emitting PbS/CdS/ZnS QDs increased to 5.6 ± 0.4 nm, with a ZnS shell thickness of 0.8 ± 0.6 nm (see transmission electron microscopy (TEM) images in the Supporting Information). The size of the PbS/CdS and PbS/CdS/ZnS QDs was determined based on TEM observations, while the PbS core size was estimated from the position of the first excitonic peak and the shell thickness was estimated by simple subtraction. Particle diameters in the sub-10 nm range are ideal for this particular type of in vivo application. These small sizes aid in the elimination of the QDs relatively easily from the body through the urine within weeks following injection, thus avoiding their undesirable accumulation in the organism.[24] It should be noted that our PbS/CdS/ZnS QDs possess an overall negative charge, determined via zeta-potential measurements (with a value of –24.2 mV at pH = 7), which likely has relevant implications with respect to their biodistribution (vide infra). Moreover, a negative zeta-potential value has a further benefit in that it helps the optical nanoprobes to avoid induced toxicity, as has been widely reported.[25] With the ZnS outer shell, our QD surface was engineered in such a way as to address a number of issues that can plague the use of PbS/CdS QDs in vivo.[26] The highly stable ZnS outer shell isolates and protects the inner PbS/CdS from the diverse biochemical and potentially aggressive environment in the live specimen that will surround the QDs postinjection thereby ensuring their stable optical properties.[27] On the other hand, the robust shell also plays a key role in imparting biocompatibility to the material by shielding the constituent heavy metals of the QDs from the organism.[27,28] This is a key novelty among Pb-based QDs as it promotes the biocompatibility and unnoticeable toxicity of our optical nanoprobes. Moreover, the MPA capping ligands help the PbS/CdS/ZnS QDs system to achieve longer circulation half-life, which can be very beneficial in future cancer-related applications as it can decisively favor their tumor uptake.[9]

2.2. Penetration Depth of Different Emitting Wavelengths

At the onset, we performed a series of experiments to address the penetration depth achievable by three slightly different PbS/CdS/ZnS QD systems in biological tissues (each of them emitting at a different wavelength). For that purpose, we designed an experimental setup to register a fluorescence fingerprint from the solution of QDs placed into a microchannel located below chicken breast tissue of variable thickness (see experimental details in the Experimental Section). Optical excitation of the QDs was achieved by using an 808 nm fiber-coupled laser diode. This excitation wavelength is ideal for in vivo bioimaging: it has been proven to be less toxic than shorter wavelengths lying within the first biological window [29] and

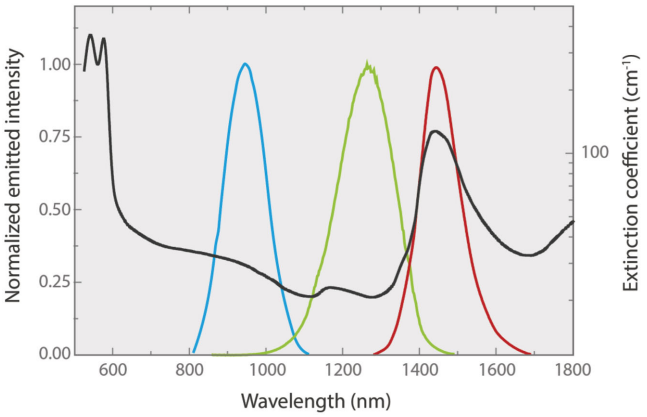

Figure 1. Spectral range of emission of different PbS/CdS/ZnS QDs. Three different emission spectra from different PbS/CdS/ZnS QDs (blue, QDs emitting at 930 nm; green, QDs emitting at 1270 nm; red, QDs emitting at 1450 nm). The black line shows the extinction coefficient (comprising both absorption and scattering contributions) of biological tissues for the spectral range under consideration; it has been conceived with diverse tissue data from references.[10,36]

at the same time, it is well known that 808 nm is much less affected by water absorption than 980 nm. The tissue penetration depths were investigated in the three NIR-emitting QDs: 930, 1270, and 1450 nm (see **Figure 1**). The three colloidal QD solutions showed highly symmetric fluorescence bands and did not show any evidence of photobleaching even during continuous illumination periods longer than 6 h and under excitation intensities as large as 4 W cm^{-2}. Figure 1 also includes the characteristic extinction coefficient of a living tissue reflecting the contribution of both inhomogeneity-induced optical scattering and optical absorption of tissue and blood components.[30] Our results demonstrated that the minimum optical extinction is found in the surroundings of 1300 nm, which suggests that the PbS/CdS/ZnS QDs emitting at approximately 1270 nm would provide the largest optical tissue penetration depth. In order to confirm this, we performed systematic subtissue imaging experiments (**Figure 2**, left side) where the outgoing fluorescence intensity generated by subtissue QDs was recorded at different tissue thicknesses (detailed information can be found in the Supporting Information). Figure 2 (right side) shows the subtissue fluorescence intensity as a function of tissue thickness as obtained for the three QDs investigated in this work. In the three cases, the subtissue fluorescence intensity showed a pseudoexponential decay. Fitting experimental data to the single exponentials gives us the *inter-wavelength penetration factor* (see the Experimental Section) following the 1/*e* criterion (where "*e*" is the base of the Naperian logarithm). Calculated in this way, the obtained value of the interwavelength penetration factor does not strongly depend on the experimental setup and, therefore, represents a rigorous and universal indicator of the penetration depth of the NIR-emitting QDs. Data analysis revealed that the largest penetration depths are, as expected from Figure 1, achieved using the 1270 nm emitting QDs (interwavelength penetration above ≈0.5 cm). Therefore, QDs emitting at 1270 nm are expected to behave as optimal bioimaging probes in a fluorescent platform, in so far as they guarantee the deepest penetration

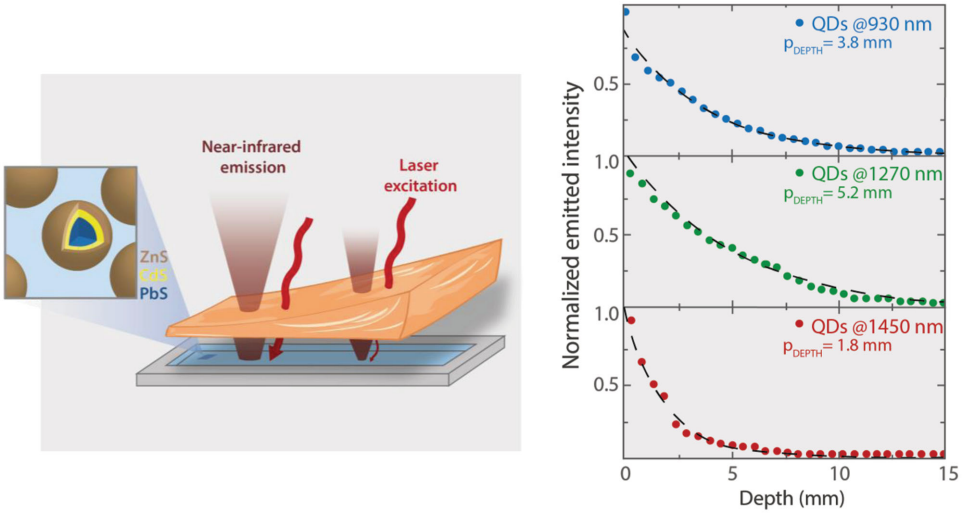

Figure 2. Scheme of the experimental procedure and penetration depths of the PbS/CdS/ZnS QDs emitting at different wavelengths. Left: experimental setup used to record the fluorescence signal from the microchannel placed below a chicken breast piece containing solutions of the three QDs under study. Right: normalized emitted intensity plotted as a function of the penetration depth on chicken breast tissue for three different emission wavelengths. Values of *inter-wavelength penetration factor* (p_{DEPTH}), as defined in the Experimental Section, are given.

in biological tissues. With our optical setup, we were able to measure maximum penetration depths close to 1.5 cm when using QDs emitting at 1270 nm.

2.3. In Vivo Imaging of Live Mice: Real-Time Biodistribution

Here, we exploit the greater optical penetration of the 1270 nm emitting QDs for real deep tissue imaging experiments in animal models. In some preliminary ex vivo imaging experiments, the signal intensity at the injected concentration saturated the acquisition camera revealing their high brightness. Therefore, for subsequent in vivo imaging experiments, we proceeded to use a significantly lower concentration of QD solution (0.04 mg mL^{-1} in phosphate-buffered saline (PBS) buffer) injected intravenously (100 µL) into the tail vein of an anesthetized mouse. The whole animal was optically excited with an 808 nm diode laser (0.1 W cm^{-2} intensity) and the NIR fluorescence generated by the QDs was recorded with a Peltier-cooled AsGaIn camera, capable of real-time image processing in the 900–1700 nm spectral range. This experimental setup has allowed us to access the dynamics of QD biodistribution and to compare this to recently published reports on fluorescent imaging using optical nanoprobes (especially QDs). Again, given the intense emission of these QDs, we were able to monitor, in real time, their in vivo-biodistribution. This experiment revealed that initially (first 0–30 s), QDs were present in the lungs (**Figure 3**, left panel, top row). However, the QDs were only transiently present in these organs as in vivo images obtained at longer times (1–2 min) revealed that accumulation finally occurs in the liver. (Figure 3, left panel, bottom row). This dynamic biodistribution pattern is demonstrated

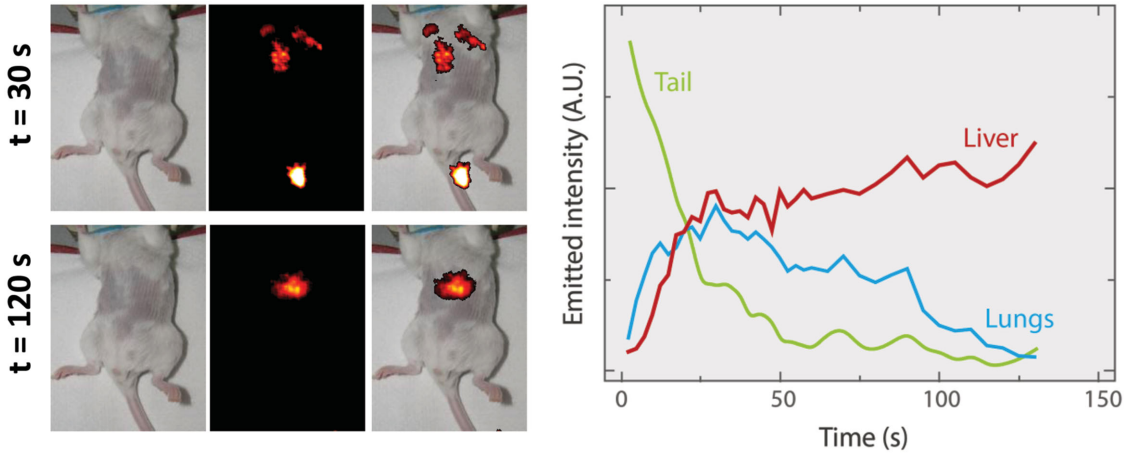

Figure 3. In vivo experiments—short-time range. Left: optical (left), fluorescence (center), and merged (right) images of the mouse taken 30 s (upper row) and 120 s (bottom row) after injection with the QD solution at a concentration of 0.04 mg mL^{-1}. Right: graph showing the evolution of the emitted intensity from three different parts of the mouse body (tail/green, liver/red and lungs/blue) as a function of time after injection.

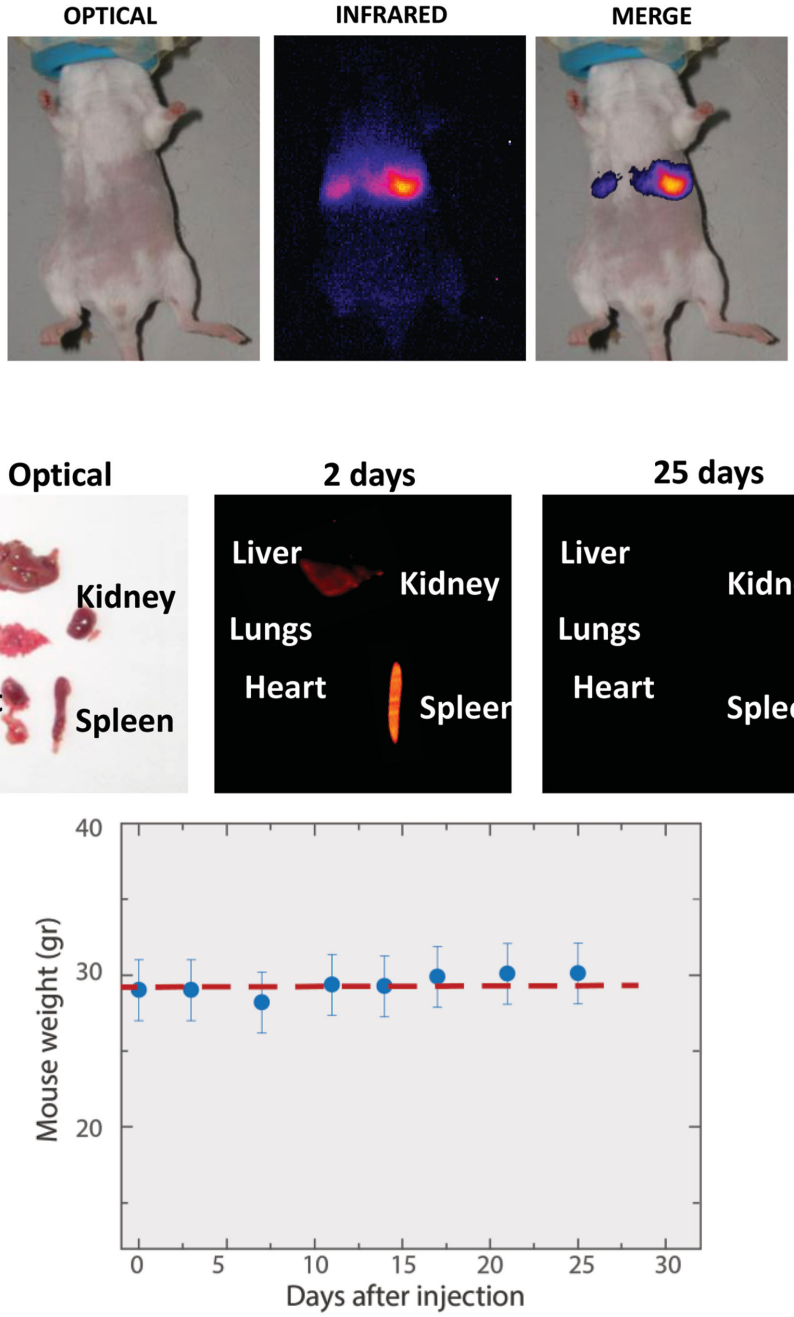

Figure 4. Ex vivo and in vivo experiments—long-time range. Top: optical (left), fluorescence (center), and merged (right) in vivo images of a mouse taken 1 min after injection of the QD solution in the bloodstream. Center: optical (left) and fluorescence (under 808 nm excitation) images taken ex vivo of five selected organs obtained from mice that were sacrificed 2 (center) or 25 days (right) after injection of the QD solution at a concentration of 0.04 mg mL^{-1}. Bottom: Bodyweight evolution during the first 25 days after the injection. Error bars are the estimated systematic error of the weighing scales. The upper panel, organs of 25 days in the middle panel, and lower panel all correspond to the same mouse.

in Figure 3, right panel, which shows the time evolution of the QD fluorescence indicating a dynamic "transfer" of QDs from lungs to liver. The detected biodistribution in the early stages after QD injection is fairly consistent with the reports previously published concerning the biodistribution of NIR-emitting QDs and carbon nanotubes.[6,14,31] Figure 3 also includes the time evolution of the fluorescence signal generated at the tail of the animal following the injection of the QDs (Figure 3, right panel). As the figure demonstrates, 100 s after injection no QDs are located at the tail indicating that they have all been distributed by the blood stream. Moreover, we have also carried out additional experiments to obtain a more accurate biodistribution in major organs at longer postinjection times (**Figure 4**). These experiments were performing by an ex vivo analysis of the different organs by sacrificing the mice at different times following intravenous injection. Data included

Table 1. Outstanding in vivo fluorescent imaging agents within the second biological windows recently reported.

System	Basic optical characteristics		Surface (chemistry and charge)		In vivo experiment		Reference
	λ_{exc}	λ_{em}	Coating/functionalization	Z-potential	Reported concentration	Power density	
Ag_2S	808 nm	≈1200 nm	6PEG	N/A	1.34 mg mL^{-1} (i.e. 0.75 nM)	0.14 W cm^{-2}	[6]
Single-walled CNTs	808 nm	Main peak ≈1200 nm	DSPE-mPEG	N/A	500 nM	0.14 W cm^{-2}	[14]
$NaYF_4$:Yb^{3+}, Er^{3+}	980 nm	1525 nm	HSA	–13.6 mV	3 nM	0.14 W cm^{-2}	[7]
RE-Doped[a] core/multishell	800 nm	1525 nm	DSPE-PEG2000-COOH	N/A	20–100 nM	0.2 W cm^{-2}	[8]
PbS/CdS/ZnS	808 nm	≈1270 nm	MPA	–24.2 mV	0.04 mg mL^{-1}	0.10 W cm^{-2}	This work

[a]The core/multishell structure is composed of: $NaGdF_4$/Na(GdYb)F_4:Er/$NaYF_4$:Yb/Er/$NaNdF_4$:Yb (from core to outer shell). PEG: polyethylene glycol; 6PEG: amine functionalized six-armed PEG; DSPE-PEG: PEGylated phospholipid; HAS: human serum albumin; DSPE-PEG2000-COOH: 1,2-distearoyl-sn-glycero-3-phosphoethanolamine-*N*-[carboxy(PEG)-2000]; MPA: mercaptopropionic acid.

in Figure 4, top panel, reveal that 1 min after injection, the QDs were mainly accumulated in the liver, lungs, and possibly in the heart as well. This is also in agreement with the in vivo results shown in Figure 3 although in this case, the signal from the heart was spatially overlapping with the signal generated by the liver. Optical evidence of QD retention was found only in the spleen 48 h after injection (Figure 4, center panel), suggesting that blood circulation has largely induced the transfer of QDs from the liver to the spleen, a phenomenon that has also been reported for other NIR-emitting nanoparticles such as neodymium-doped SrF_2 nanoparticles.[32] Finally, when the organs were analyzed 25 days postinjection, no evidence of QD presence was found at all, very likely suggesting complete elimination of the QDs by, most probably, the urine. This fact is in agreement with our toxicity studies revealing that no signs of adverse effects were observed in injected mice even for observation times as long as 25 days where their behavior did not appreciably change over this time span (see Figure 4, bottom panel, that includes the time evolution of mouse weight after intravenous injection of our QDs). The absence of related toxicity of our QDs has also been determined in in vitro toxicity experiments. Figure S5 of the Supporting Information shows the cytotoxicity results obtained in HeLa cancer cells after systematic incubation with our NIR-emitting QDs, revealing a negligible toxicity, thus confirming that the biocompatible ZnS shell is isolating the heavy metals from the biological milieu. Furthermore, any heavy metal leaching is less likely to occur since high-energy UV light is not used to optically excite the QDs. Clearly, future experiments on these novel NIR-emitting QD nanoprobes will tackle the issue of their circulation time in the body and strategies to minimize their rapid accumulation in the liver and spleen. We must comment at this point that the phenomenon of accumulation in the liver and spleen is, very likely, connected to the negative surface charge of the QDs, (Z-potential value of –24.2 mV as reported above). As a matter of fact, it has been recently reported that when injecting visible-emitting negatively charged CdSe/ZnS QDs, preferential accumulation in the liver seems to be generally observed,[33] although slight accumulation in the spleen and kidney could also be possible. Future work will focus on the surface engineering of the QDs to avoid the accumulation in the liver opening the door for long circulation times that could lead, for instance, to tumor targeting. Taking all this into account, the PbS/CdS/ZnS QDs reported here offer the real possibility of using a remarkably diluted solution when compared to other NIR-emitting optical nanoprobes proposed for in vivo imaging purposes,[5] thus reducing the amount of QDs required for injection into the living specimen. This clearly implies a lower associated risk, in the form of accumulation of QDs in the body. Finally, we must point out that a full toxicological study must be carried out to further assess their long-term toxicity.

We should explicitly state that as a result of the high-emission intensity of these NIR-emitting QDs, remarkably low values of both QD solution concentration and excitation power density were required throughout the experiments described in the following paragraphs. Thus, **Table 1** shows a comparative narrative of the technical features of some of the most outstanding results achieved for in vivo fluorescence imaging in the second biological window, using different types of nanomaterial platforms, such as lanthanide-based nanoparticles, single-walled carbon nanotubes (CNTs), and silver sulfide (Ag_2S).[6–8,14] These are critical parameters that must be accounted for in any in vivo imaging platform if any aspiration exists of bringing the technology from the bench to the bedside. The significance of reducing both the amount of foreign agents to be injected in a live specimen and the intensity of the excitation laser beam allows us to place our PbS/CdS/ZnS QDs among the best of the high-penetration in vivo fluorescence imaging nanoprobes. It is abundantly clear that high QD concentration and intense laser beams could have potentially harmful and even potentially life threatening consequences for the treated animal. Therefore, it must be pointed out again that the QDs developed in this work have been repeatedly tested for in vivo imaging using 100 µl of an extremely low concentration PBS solution (0.04 mg mL^{-1}), a value that is two orders of magnitude lower than, for instance, the concentration reported (200 µl of a 1.34 mg mL^{-1} concentrated solution) in the widely known work by Hong et al,[6] on Ag_2S QDs as in vivo NIR imaging nanoprobes.

2.4. Nanothermometry

Once their potential use as highly penetrating in vivo fluorescence probes had been demonstrated, we also evaluated the

possible application of the 1270 nm emitting QDs as thermal sensors. The emission intensity was measured and plotted as a function of temperature (**Figure 5**a) and the spectra of a colloidal solution of QDs obtained at two different temperatures are shown in the inset. It is clear that the fluorescence intensity is linearly dependent on temperature. A sensitivity of 1% per °C has been obtained from the linear fit of experimental data in the biological temperature range. Both the linearity of this

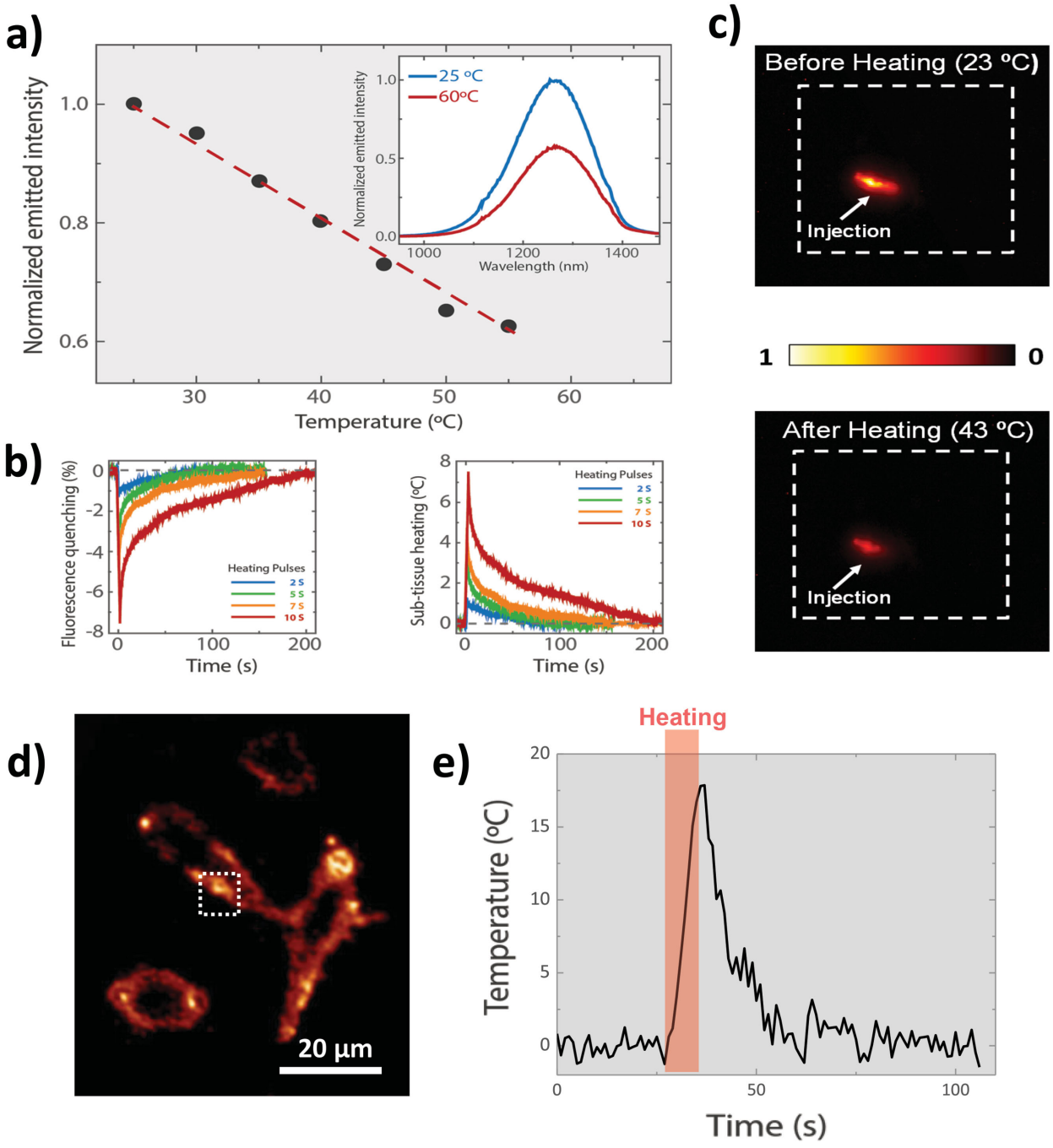

Figure 5. a) Emission intensity (normalized by the values measured at room temperature) collected from QDs emitting at 1270 nm as a function of the induced temperature of the solution. The inset shows two spectra recorded at the two extreme values (25 and 60 °C) of the temperature span studied. b) Intensity recorded versus time from the QDs after heating the chicken breast tissue using short hot-air pulses. The time evolution of the fluorescence quenching (left graph) can be translated into the corresponding time evolution of the subtissue heating process (right side graph), from the calibration shown in Figure 5a. c) Subtissue fluorescence images taken at two different temperatures from the chicken breast previously injected with QDs emitting at 1270 nm. d) Fluorescence image of four HeLa cells, upon their excitation with an 808 nm laser diode. Cells had been previously incubated with a solution of 1270 nm emitting QDs (left). Continuous monitoring of the temperature of the HeLa cells before, during, and after a 10s heat pulse, as a function of time (right); white dashed square in the figure at the left shows the area under temperature monitoring.

thermo-optical behavior and the obtained value of the thermal sensitivity constitute two remarkable features of these QDs. The combination of these two properties suggests the use of our NIR-emitting QDs as reliable thermal nanosensors for biomedical applications. At this point, it is important to remark that the shape and the position of the emission spectra recorded in the physiological temperature range showed no significant variations and remained almost unchanged, at variance with the visible-emitting CdSe and CdTe QDs previously used as in vivo nanosized thermal sensors[34] The strong temperature-dependent emission intensity variation of our QDs was found to be completely reversible without evidence of morphological/structural changes for temperatures varying between 20–70 °C, which includes the range of biological interest. The thermal sensitivity parameter S, defined as

$$S = \frac{1}{I_0}\frac{\mathrm{d}I}{\mathrm{d}T} \quad (1)$$

(I, T, and I_0 are the emitted fluorescence intensity, temperature, and emitted fluorescence intensity at room temperature, respectively) can be estimated from data included in Figure 5a, to be $S = 1 \times 10^{-2}$ °C^{-1}. When comparing this sensitivity to the thermal sensitivities previously reported for other ratiometric fluorescent nanothermometers[27,35], we find the best nanothermometers have S values in the range ~2×10^{-2} °C^{-1}, however, most of these works have focused only in the visible domain. Indeed, the best reported sensitivities for NIR-emitting fluorescent nanothermometers reported to date are not larger than $S = 2.5 \times 10^{-3}$ °C^{-1}. The NIR-emitting QDs reported herein provide a thermal sensitivity improvement larger than one order of magnitude, constituting a significant step toward high-resolution real subtissue temperature sensing.[35]

The actual capabilities of our QDs for fluorescence thermal sensing have been demonstrated by first performing ex vivo experiments. In doing so, QDs were injected at a depth of 1 cm into chicken breast tissue. The fluorescence intensity was monitored in real-time while subjecting the tissue to various cooling and heating treatments of different durations. A proper analysis of the time evolution of the subtissue located QDs allowed us to access the time evolution of the subtissue temperature, i.e., we were able to record, for the first time to the best of our knowledge, subtissue thermal transients with a subdegree thermal resolution, as can be observed in Figure 5b. The fluorescence images of the chicken breast after heating and cooling treatments are included in Figure 5c, which clearly shows how the subtissue fluorescence intensity increases after a cooling cycle and decreases after a heating cycle. The potential application of our QDs for thermal sensing in biosystems has been further corroborated by performing in vitro experiments. In doing so, HeLa cancer cells were incubated with our QDs. NIR fluorescence images (shown in Figure 5d, left side) demonstrated an efficient incorporation of QDs into HeLa cells. Experimental details regarding NIR cell imaging can be found in the Experimental Section. The HeLa cells were subjected to a 10 s heating pulse provided by a micro air-heater, and the time evolution of the cell´s temperature was inferred from the time evolution of the QD fluorescence. Time evolution of the cell's temperature before, during, and after the heating pulse is shown in Figure 5d, (right side). The fast heating and subsequent slow thermal relaxation of HeLa cells is clearly shown, demonstrating the exciting potential application of these QDs for thermal sensing at the cellular level. These QDs have the capability to not only act as nanothermometers but can compete in NIR-nanothermometry sensitivity with the current state of the art. Moreover, this adds another dimension (or modality) to these already intense NIR-emitting nanoprobes. To our knowledge we are the first to report the first fluorescent nanothermometers with such a sensitivity emitting within the second biological window, thus accounting for their higher penetration depth in comparison to any of the previously reported fluorescent nanothermometers.

3. Conclusion

In summary, we have developed a QD-based imaging system based on NIR-emitting PbS/CdS/ZnS QDs with minimal noticeable toxicity that, through careful engineering of their emission wavelength, allowed us to obtain fluorescence imaging nanoprobes with optimal penetration depths in biological tissue. This was achieved by the combination of an excitation wavelength (808 nm) lying within the first biological window coupled with an emitted fluorescence signal lying in the second biological window (1270 nm), which takes advantage of the minimized scattering from biological tissues at these long wavelengths. Additionally, this new platform exhibited multifunctionality beyond their use as pure imaging nanoprobes. The system is capable of acting as a biological nanothermometer, based on the reliable thermal-dependent behavior of the fluorescence signal. The PbS/CdS/ZnS QDs studied here can easily be exploited to obtain thermal mapping of subskin areas in live specimens, an accomplishment of great relevance for early disease detection and also for real-time therapy monitoring. Moreover, as a result of the intense signal provided by the NIR-emitting QDs, we are able to elucidate the real-time biodistribution of the QDs by means of in vivo experiments in live mice. We determined the lack of detectable chemical toxicity attributed to the QDs based on cell culture assays, as well as the lack of adverse health effects (no significant weight changes or behavior abnormalities were found over 4 weeks) for mice injected with a low concentration of QDs, coupled with the absence of any fluorescence signal detected in the body organs at the end of the experiment. We can therefore ascertain that the ZnS outer shell imparts a great deal of biocompatibility and stability of the PbS/CdS/ZnS QDs reported here. Also, the intense fluorescent emission of this material allows for low doses to be used, significantly improving the current state of the art. This greatly diminishes the likelihood of causing adverse health effects on the live specimen when used as optical bioimaging probes.

Following further surface engineering, a number of prospective avenues open up for these PbS/CdS/ZnS QDs in the realm of NIR imaging. For example, modification of the surface charge could lead to an increase in the circulation half-life in the living specimen. In this case, nontargeting tumor imaging can be expected, especially when taking into

account the mechanical retention mechanisms that can contribute to the accumulation of the QDs in the designated areas. Another possibility is to chemically functionalize the QDs to expressly target different cancer tumors. Due to their small sizes, the possibility exists that they can reach a variety of body organs. In both of these cases, the high brightness of the QDs allow for the application of low injection doses thereby mitigating the risk of any nanoparticle-related adverse effects while benefiting their deep tissue penetration capabilities for NIR imaging and nanothermometry tracking. These two modalities can be very useful for real-time monitoring during ongoing therapy.

4. Experimental Section

Synthesis of Water Dispersible PbS/CdS/ZnS QDs: The PbS/CdS/ZnS core/shell/shell QDs with MPA as the capping ligand were prepared as described below. The synthesis details of the PbS core and PbS/CdS core/shell are provided in the Supporting Information. Coating the PbS/CdS QDs cores with a ZnS shell and replacing the oleic acid (OA) by MPA so as to impart water dispersibility were achieved simultaneously. In a typical reaction, 0.02 g phosphorous pentasulfide, 0.5 g MPA, and 0.3 mL butylamine were heated at 110 °C for 20 min in 10 mL 1-methyl-2-pyrrolidinone (NMP) in a sealed vial to dissolve the sulfide. In a separate vial, 0.07 g zinc chloride, 0.5 g MPA, and 0.3 mL butylamine were mixed in 10 mL NMP and heated to dissolve in the same way. After cooling down to room temperature, 0.007 g of OLA-capped PbS/CdS particles were dissolved in the phosphorous pentasulfide solution, and the whole solution was mixed with the zinc chloride solution. The mixture solution was heated at 70 °C for 30 min in a microwave oven (Discover; CEM corporation), yielding the MPA-capped PbS/CdS/ZnS core/shell/shell QDs. The PbS/CdS/ZnS core/shell/shell QDs were purified by repeated centrifugation/redispersion four times using hexane, the purified QDs were dried overnight at room temperature under vacuum and dispersed in water. The water dispersible QDs were further treated by ultrafiltration using an Ultracel-15 centrifugal filter (Millipore) three times and redispersed in PBS solution, and the pH of the solution was adjusted to 7.5 by adding NaOH solution.

Postsynthesis QD Characterization: The PbS/CdS and PbS/CdS/ZnS QDs were characterized by TEM (JEOL 2100F). Absorption spectra were acquired using a Cary 5000 UV–vis–NIR spectrophotometer (Varian Cary 5000) with a scan speed of 600 nm min^{-1}. Both absorption spectra and TEM image are shown in Figure S1 of the Supporting Information. Fluorescence experiments were carried to determine the final NIR emission wavelength of the PbS/CdS/ZnS and were obtained with a Fluorolog®-3 system (Horiba Jobin Yvon) using a photomultiplier tube detector. The excitation wavelength was set at 670 nm. The size of the PbS QDs or PbS cores was calculated based on the first exciton absorption peak. The zeta-potential of the as-synthesized PbS/CdS/ZnS QDs was measured by using a DLS instrument (Malvern, Nano-ZS).

Fluorescence Signal Interwavelength Penetration Depth: A series of experiments were performed to address the penetration depth achievable by the PbS/CdS/ZnS QDs in biological tissues. We designed an experimental setup to register a fluorescence signal emanating from a microchannel, filled with a solution of QDs in PBS, which was placed underneath a piece of chicken breast. The chicken tissue was cut in a triangular shape that allowed us to establish a geometrical correspondence between the longitudinal emission intensity profile and the penetration depth of the out coming NIR photons. The signal was recorded by a Xeva-1.7 infrared camera (Xenics Inc.), capable of detecting fluorescence emission in the 900–1700 nm spectral range. The QD solution in the microchannel, emitting at three different wavelengths (930, 1270, and 1450 nm), were optically pumped by a fiber diode at 808 nm (LIMO Inc), using a broad field noncollimated optical configuration.

The value for the *interwavelength penetration factor* (p_{DEPTH}) in Figure 2a is the fitting parameter d from the well-known exponential Lambert–Beer equation

$$y = C \times \exp\left(\frac{-x}{d}\right) + y_0 \quad (2)$$

In this way, we can obtain a reliable value for comparing several "relative" penetration depths achieved by using different emission wavelengths, thus omitting any experimental perturbation that does not contain any meaningful physical significance. From equation (2), we take p_{DEPTH} as the fitting parameter d, i.e., when the emitted intensity signal decreases to a *1/e* of the initial (tissue surface) value (see Supporting Information for a full identification of the different coefficients of the equation).

Cell Imaging and Nanothermometry: HeLa cells were incubated with QDs emitting at 1270 nm (as described in the Supporting Information). Wide-field illumination was provided by an uncollimated fiber–laser diode operating at 808 nm (LIMO Inc) that was optically coupled to an inverted Olympus CS-38 microscope. The fluorescence signal generated by intracellular incorporated QDs was collected with a 50X infrared Olympus microscope objective and recorded by a Xeva-1.7 infrared camera (Xenics Inc.) coupled to the inverted microscope. Residual 808 nm radiation was blocked by using a set of longpass fluorescence filters with cutoff wavelength of 1000 nm. In these experimental conditions, the infrared camera built up the fluorescence image by displaying the integrated intensity generated by QD in the 1000–1700 nm spectral range.

In Vivo Experiments Using Mice: For all in vivo experiments, 7 week old female CD1 mice were injected with a solution of QDs in PBS. For the in vivo imaging, the previously shaved mice were anesthetized with 2% isoflurane. The description of the imaging system can be found in the Supporting Information. Although the injected volume was always 100 µl, the concentration of QDs in PBS (0.04 mg mL^{-1}; 0.2 mg mL^{-1}) and location of the injection to access the bloodstream (retro-orbital sinus; tail vein) varied among experiments. All animal husbandry and experimental procedures were conducted in compliance with 2010/63/UE European guidelines and were approved by the Ethics Committee for Research of Universidad Autónoma de Madrid (Comité Ético para la Investigación, CEI), in the frame of the project FIS-PI12/01253 supported by the Spanish Ministerio de Economía y Competitividad.

Supporting Information

Supporting Information is available from the Wiley Online Library or from the author.

Acknowledgements

A.B., F.R., and E.C. contributed equally to this work. A.B. thanks the Fonds de recherche du Québec-Nature et Technologies (FRQNT) and the Canadian Institutes of Health Research–Breast Cancer Society of Canada (CIHR-BCSC) for postdoctoral funding through the Programme de Bourses d'Excellence and an Eileen Iwanicki Fellowship in Breast Cancer Imaging, respectively. F.R. greatly appreciates financial support from the Merit Scholarship Program for Foreign Students from the Ministére de L'Education, du Loisir et du Sport du Québec (MELS). F.V. and D.M. are grateful to the Natural Sciences and Engineering Research Council of Canada (NSERC) and FRQNT for funding. F.V. wholeheartedly thanks the Foundation Sibylla Hesse for supporting his research. D.M. also thanks the Quebec Center for Functional Materials for support. This work was also supported by Spanish Ministerio de Economia y Competitividad under projects MAT2010–16161 and MAT2013–47395-

C4–1-R. The authors wish to thank biocellavi.com for assistance in the preparation of the figures.

Received: June 27, 2015
Revised: July 18, 2015
Published online: October 6, 2015

[1] a) G. Choy, P. Choyke, S. K. Libutti, *Mol. Imaging* **2003**, *2*, 303; b) E. M. Hillman, C. B. Amoozegar, T. Wang, A. F. McCaslin, M. B. Bouchard, J. Mansfield, R. M. Levenson, *Philos. Trans. R. Soc., A* **2011**, *369*, 4620.

[2] P. A. Jarzyna, A. Gianella, T. Skajaa, G. Knudsen, L. H. Deddens, D. P. Cormode, Z. A. Fayad, W. J. M. Mulder, *Wiley Wiley Interdiscip. Rev.: Nanomed. Nanobiotechnol.* **2010**, *2*, 138.

[3] a) H. S. Jensen, F. O. Andersen, *Limnol. Oceanogr.* **1992**, *37*, 577; b) A. R. Cossins, K. Bowler, *Temperature Biology of Animals*, Chapman and Hall, London, UK **1987**; c) C. Stefanadis, C. Chrysochoou, D. Markou, K. Petraki, D. B. Panagiotakos, C. Fasoulakis, A. Kyriakidis, C. Papadimitriou, P. K. Toutouzas, *J. Clin. Oncol.* **2001**, *19*, 676; d) B. Hildebrandt, P. Wust, O. Ahlers, A. Dieing, G. Sreenivasa, T. Kerner, R. Felix, H. Riess, *Crit. Rev. Oncol. Hematol.* **2002**, *43*, 33.

[4] A. Choi, D. Maysinger, in *Semiconductor Nanocrystal Quantum Dots*, (Ed: A. Rogach), Springer, Vienna, Austria **2008**, 349.

[5] K. Yang, S. Zhang, G. Zhang, X. Sun, S.-T. Lee, Z. Liu, *Nano Lett.* **2010**, *10*, 3318.

[6] G. Hong, J. T. Robinson, Y. Zhang, S. Diao, A. L. Antaris, Q. Wang, H. Dai, *Angew. Chem.* **2012**, *124*, 9956.

[7] D. Naczynski, M. Tan, M. Zevon, B. Wall, J. Kohl, A. Kulesa, S. Chen, C. Roth, R. Riman, P. Moghe, *Nat. Commun.* **2013**, *4*, 2199.

[8] R. Wang, X. Li, L. Zhou, F. Zhang, *Angew. Chem.* **2014**, *126*, 12282.

[9] J. Gao, K. Chen, R. Xie, J. Xie, S. Lee, Z. Cheng, X. Peng, X. Chen, *Small* **2010**, *6*, 256.

[10] A. M. Smith, M. C. Mancini, S. Nie, *Nat. Nanotechnol.* **2009**, *4*, 710.

[11] a) C. R. Simpson, M. Kohl, M. Essenpreis, M. Cope, *Phys. Med. Biol.* **1998**, *43*, 2465; b) E. Salomatina, B. Jiang, J. Novak, A. N. Yaroslavsky, *J. Biomed. Opt.* **2006**, *11*, 064026; c) S.-H. Tseng, A. Grant, A. J. Durkin, *J. Biomed. Opt.* **2008**, *13*, 014016.

[12] a) N. Won, S. Jeong, K. Kim, J. Kwag, J. Park, S. G. Kim, S. Kim, *Mol. Imaging* **2012**, *11*, 338; b) E. J. Henderson, A. J. Shuhendler, P. Prasad, V. Baumann, F. Maier-Flaig, D. O. Faulkner, U. Lemmer, X. Y. Wu, G. A. Ozin, *Small* **2011**, *7*, 2507; c) J.-C. Boyer, M.-P. Manseau, J. I. Murray, F. C. J. M. van Veggel, *Langmuir* **2009**, *26*, 1157.

[13] a) Y. T. Lim, S. Kim, A. Nakayama, N. E. Stott, M. G. Bawendi, J. V. Frangioni, *Mol. Imaging* **2003**, *2*, 50; b) Y. Zhang, G. Hong, Y. Zhang, G. Chen, F. Li, H. Dai, Q. Wang, *ACS Nano* **2012**, *6*, 3695; b) N. Venkatachalam, T. Yamano, E. Hemmer, H. Hyodo, H. Kishimoto, K. Soga, *J. Am. Ceram. Soc.* **2013**, *96*, 2759; c) E. Hemmer, N. Venkatachalam, H. Hyodo, A. Hattori, Y. Ebina, H. Kishimoto, K. Soga, *Nanoscale* **2013**, *5*, 11339.

[14] K. Welsher, S. P. Sherlock, H. Dai, *Proc. Natl. Acad. Sci. USA* **2011**, *108*, 8943.

[15] D. R. Lide, *CRC Handbook of Chemistry and Physics*, CRC Press, Boca Raton, FL, USA **2004**.

[16] F. C. J. M. van Veggel, *Chem. Mater.* **2013**, *26*, 111.

[17] a) R. Koole, G. Allan, C. Delerue, A. Meijerink, D. Vanmaekelbergh, A. J. Houtepen, *Small* **2008**, *4*, 127; b) D. K. Smith, J. M. Luther, O. E. Semonin, A. J. Nozik, M. C. Beard, *ACS Nano* **2010**, *5*, 183.

[18] M. A. Hines, G. D. Scholes, *Adv. Mater.* **2003**, *15*, 1844.

[19] Y. Nakane, Y. Tsukasaki, T. Sakata, H. Yasuda, T. Jin, *Chem. Commun.* **2013**, *49*, 7584.

[20] F. Ren, H. Zhao, F. Vetrone, D. Ma, *Nanoscale* **2013**, *5*, 7800.

[21] a) D. F. Flick, H. F. Kraybill, J. M. Dlmitroff, *Environ. Res.* **1971**, *4*, 71; b) B. L. Vallee, D. D. Ulmer, *Annu. Rev. Biochem.* **1972**, *41*, 91.

[22] L. Ye, K.-T. Yong, L. Liu, I. Roy, R. Hu, J. Zhu, H. Cai, W.-C. Law, J. Liu, K. Wang, J. Liu, Y. Liu, Y. Hu, X. Zhang, M. T. Swihart, P. N. Prasad, *Nat. Nanotechnol.* **2012**, *7*, 453.

[23] T. Zhang, H. Zhao, D. Riabinina, M. Chaker, D. Ma, *J. Phys. Chem. C* **2010**, *114*, 10153.

[24] a) J.-W. Yoo, E. Chambers, S. Mitragotri, *Curr. Pharm. Des.* **2010**, *16*, 2298; b) H. S. Choi, W. Liu, P. Misra, E. Tanaka, J. P. Zimmer, B. I. Ipe, M. G. Bawendi, J. V. Frangioni, *Nat. Biotechnol.* **2007**, *25*, 1165.

[25] a) C. Chouly, D. Pouliquen, I. Lucet, J. J. Jeune, P. Jallet, *J. Microencapsulation* **1996**, *13*, 245; b) Y. Tang, S. Han, H. Liu, X. Chen, L. Huang, X. Li, J. Zhang, *Biomaterials* **2013**, *34*, 8741.

[26] A. M. Derfus, W. C. W. Chan, S. N. Bhatia, *Nano Lett.* **2003**, *4*, 11.

[27] E. Carrasco, B. del Rosal, F. Sanz-Rodríguez, Á. J. de la Fuente, P. H. Gonzalez, U. Rocha, K. U. Kumar, C. Jacinto, J. G. Solé, D. Jaque, *Adv. Funct. Mater.* **2015**, *25*, 615.

[28] C. Kirchner, T. Liedl, S. Kudera, T. Pellegrino, A. Muñoz Javier, H. E. Gaub, S. Stölzle, N. Fertig, W. J. Parak, *Nano Lett.* **2004**, *5*, 331.

[29] a) H. Liang, K. T. Vu, P. Krishnan, T. C. Trang, D. Shin, S. Kimel, M. W. Berns, *Biophys. J.* **1996**, *70*, 1529; b) K. König, in *Handbook of Biological Confocal Microscopy*, (Ed: J. B. Pawley), Springer Science+Business Media, LLC, New York, NY, USA **2006**.

[30] W.-F. Cheong, S. A. Prahl, A. J. Welch, *IEEE J. Quantum Electron.* **1990**, *26*, 2166.

[31] Y. Zhang, Y. Zhang, G. Hong, W. He, K. Zhou, K. Yang, F. Li, G. Chen, Z. Liu, H. Dai, *Biomaterials* **2013**, *34*, 3639.

[32] I. Villa, A. Vedda, I. Cantarelli, M. Pedroni, F. Piccinelli, M. Bettinelli, A. Speghini, M. Quintanilla, F. Vetrone, U. Rocha, C. Jacinto, E. Carrasco, F. Rodríguez, Á. Juarranz, B. del Rosal, D. Ortgies, P. Gonzalez, J. Solé, D. García, *Nano Res.* **2014**, *8*, 649.

[33] Y. Tang, S. Han, H. Liu, X. Chen, L. Huang, X. Li, J. Zhang, *Biomaterials* **2013**, *34*, 8741.

[34] a) L. M. Maestro, E. M. Rodriguez, F. S. Rodriguez, M. C. I. la Cruz, A. Juarranz, R. Naccache, F. Vetrone, D. Jaque, J. A. Capobianco, J. G. Sole, *Nano Lett.* **2010**, *10*, 5109; b) L. M. Maestro, J. E. Ramirez-Hernandez, N. Bogdan, J. A. Capobianco, F. Vetrone, J. G. Sole, D. Jaque, *Nanoscale* **2012**, *4*, 298.

[35] A. Benayas, B. del Rosal, A. Pérez-Delgado, K. Santacruz-Gómez, D. Jaque, G. A. Hirata, F. Vetrone, *Adv. Opt. Mater.* **2015**, *3*, 687.

[36] S. L. Jacques, *Phys. Med. Biol.* **2013**, *58*, R37.